Analysis of the microstructure and morphology of disordered kaolinite based on the particle size distribution

Yongjie Yang, Maguy Jaber, Laurent Michot, Baptiste Rigaud, Philippe Walter, Lucie Laporte, Kenan Zhang, Qinfu Liu

Version of Record: https://www.sciencedirect.com/science/article/pii/S0169131722003969
Manuscript_bfe0d67de13e6a1e6886f9f2402664d1

Analysis of the microstructure and morphology of disordered kaolinite based on the particle size distribution

Yongjie Yang[a,b], Maguy Jaber[b,*], Laurent J. Michot[c], Baptiste Rigaud[d], Philippe Walter[b], Lucie Laporte[b], Kenan Zhang[a], Qinfu Liu[a,*],

[a] School of Geoscience and Surveying Engineering, China University of Mining and Technology (Beijing), 100083, Beijing, China

[b] Laboratoire d'Archéologie Moléculaire et Structurale (LAMS), UMR 8220, CNRS， Sorbonne Université, Case Courrier 225, UPMC 4 Place Jussieu, 75005, Paris, France

[c] Laboratoire PHENIX, UMR 8234, CNRS, Sorbonne Université, UPMC, 4 Place Jussieu, 75005, F-75252 Paris, France

[d] CNRS Institut des Matériaux de Paris Centre (FR2482), Sorbonne Université, 4 Place Jussieu, 75005, Paris, France

* Corresponding author

Email: maguy.jaber@upmc.fr (M. Jaber), lqf@cumtb.edu.cn (Q. Liu)

Abstract:

The defected kaolinite is common in sedimentary kaolin, but its structure and disorder mechanism remains unclear. In this paper, three different size distributions of kaolinite particles: 0~300 nm, 200~1000 nm, and 500~2000 nm, were separated and classified from high-defect sedimentary kaolin, collected from Quaternary sedimentary kaolin in Guangxi Zhuang Autonomous Region of China. The three particle sizes of kaolinite have been monitored by particle size analyzer, high-resolution magic-angle spinning NMR (MAS NMR), small and wide-angle X-ray scattering (SAXS and WAXS), X-ray diffraction (XRD), BET surface analyzer, nitrogen gas-adsorption, scanning electron microscopy (SEM), and high-resolution transmission electron microscopy (HRTEM). The results revealed that the smallest particle size of kaolinite exhibited high degrees of broken Al-O-Al and Si-O-Si bonds, more disordered structure, and elevated specific surface area. The degree of the structural disorder of kaolinite increases as the particle size decreases, which can be attributed to the more aluminum substituted for silicon in tetrahedron sheet in the finer kaolinite crystal, compared to the coarser kaolinite crystals.

Keywords: Disordered kaolinite, Particle size distribution, Microstructure, NMR, SAXS, WAXS

1. Introduction

Kaolinite, $Al_2Si_2O_5(OH)_4$, with the unit cell parameters: a_0=0.517 nm，b_0=0.898 nm, c_0=0.735 nm, α=91.68°, β=105.12°, γ=89.75° (Richard and Rendtorff, 2019), is a 1:1 layered dioctahedral hydrous aluminosilicate that generally exhibits structural order and disorder in nature (Awad et al., 2018; Bish, 1993; Brindley et al., 1986). Silicon atoms are organized as ditrigonal rings of silicon-oxygen tetrahedra and form the tetrahedral sheet. In contrast, aluminum atoms are organized as aluminum-oxygen octahedra in the octahedral sheet that also contains one-third of empty octahedral voids, which maintains the electrical balance of the whole structure. Kaolinite is then an uncharged structure, even if some samples bear a small permanent negative charge due to the existence of isomorphic substitutions in either the tetrahedral or octahedral sheet. Numerous authors have debated the origin of structural disorder in kaolinite. It was supposed that disorder in kaolinite is caused by substituting cations within the lattice, such as replacing Al^{3+} with Fe^{3+} in alumina octahedral sheet or Si^{4+} substituted by Al^{3+} in silica tetrahedral sheet (Brindley et al., 1986; Newman et al., 1994). The second reason for the structural disorder

was suggested that the translation between adjacent layers, which is related to the pseudo-mirror plane, coincident with the long diagonal of the unit cell (Plançon et al., 1989). The third possibility relies on the existence of interlayer shifts between two adjacent layers. There are two types of shifts: $\boldsymbol{t_1}$ and $\boldsymbol{t_2}$, where $\boldsymbol{t_1}$ is a shift of (~-$\boldsymbol{a}$/3) and $\boldsymbol{t_2}$ (~-$\boldsymbol{a}$/3+$\boldsymbol{b}$/3). Such alternating $\boldsymbol{t_1}$ and $\boldsymbol{t_2}$ shifts were observed by High-Resolution Transmission Electron Microscopy (HRTEM) by Kogure et al. (2010) in sedimentary kaolinite from Brasil. These three types of defects broaden the reflections observed by X-Ray Diffraction (XRD). They particularly affect the (02*l*) and (11*l*) sequences (20-23° 2θ, using Cu*K*α), and the (13*l*) and (20*l*) sequences (35-40° 2θ, using Cu*K*α) (Aparicio, 1999).

The question of the link between kaolinite particle size distribution (PSD) and the extent of disorder in the structure remains somehow open. A better understanding of the potential relationships between disorder and particle size would provide relevant information to better assess the geological processes that control the composition of kaolinite formed during weathering and, therefore, yield data about the geological background at the time of mineralization (Varajão et al.,

79 2001).

80 The particle size of kaolinite platelets is generally < 2 μm (equivalent
81 sphere diameter). Suspensions of kaolinite fine particles display low
82 viscosity (Rand and Melton, 1977), better rheological behavior (Gupta
83 et al., 2011; Mpofu et al., 2003), and anti-flocculation performance
84 (Du et al., 2010). It is worth pointing out that the size of kaolinite
85 particles used commercially is generally less than 2 μm, such as paper
86 coating kaolin, where 70~90% of the particles used are less than 2 μm
87 (Morsy et al., 2014; Silva et al., 2009). Even finer particles less than 1
88 μm used for high-performance thermal shock resistance ceramics
89 (Kobayashi et al., 2000), and 300 nm for high reinforcement of
90 polymer filler (Zhang et al., 2021a; Zhang et al., 2010). Most
91 advanced applications of kaolinite derive from its versatility in terms
92 of particle size, morphology, and microstructure (Jaber et al., 2018;
93 Liu et al., 2021; Yang et al., 2020; Zhang et al., 2017; Zhang et al.,
94 2021b). Microstructural features play a significant role in determining
95 some of the physical and mechanical properties of kaolinite (i.e.,
96 thermal resistance and deformation indices). Still, until now, little
97 research has been carried out to investigate the effect of kaolinite PSD

on microstructure and micromorphology. One of the main reasons is likely related to the difficulties associated with controlling natural kaolinite particle size.

Wet sieving and pipette methods are the primary ways to assess the particle size distribution of clay minerals (Konert and Vandenberghe, 1997; Wen et al., 2002; Yang et al., 2015), but mainly suitable for sizes ranged from 50 to 2000 μm. For smaller particles and especially for particles lower than 2 μm, the sedimentation-based pipette method (SPM) is commonly used. The pipette method defines the particles as the size of a sphere that settles in the liquid at the same sedimentation velocity, supported by Stokes' law (Cheng and Schachman, 1955; Yang et al., 2015). However, based on Stokes' law, it will take 180 h to separate the < 1 μm part for a kaolinite suspension with a viscosity less than 5.7 mpa·s. It is time-consuming for the ultrafine part, and the results are increasingly unreliable because of the effect of Brownian motion on the rate of sedimentation (Eshel et al., 2004).

Mechanical grinding, such as ball and planetary milling, was used to generate ultrafine kaolinite particles (Hamzaoui et al., 2015; Makó et al., 2001; Suraj et al., 1997). However, elevated grinding times will

117 destroy the kaolinite structure. Another option for decreasing particle
118 size is to perform sonication, however, delamination induced by
119 ultrasonics increases the (-1/3***a***+1/3***b***) translation disorder (Franco et
120 al., 2004a), and the Hinkley Index (HI) correspondingly decreases
121 from 1.19 to 0.53 (Franco et al., 2004b). Although grinding and
122 ultrasonication can yield very fine kaolinite particles, the products bear
123 numerous non-natural disorder structures. Consequently, such
124 treatments are not adequate for studying the disordered structure of
125 natural ultrafine kaolinite.
126 Bearing this in mind, the objective of the present paper is three-fold: (1)
127 to separate three classes of kaolinite particles under 2 μm, to yield
128 "ultrafine" (< 300 nm), "intermediate" (200~1000 nm), and "coarse
129 particles" (500~2000 nm); (2) to examine the microstructure and
130 micromorphology of the three particle sizes of kaolinite; (3) to
131 postulate a mechanism of the structural disorder and verify it through
132 NMR and XRD experiments.

133 2. Materials and methods

134 2.1 Materials

135 The sample used for this study was a high-defect ("poor-crystallized")

kaolinite with a Hinckley Index of 0.175, collected from Quaternary sedimentary kaolin in Guangxi Zhuang Autonomous Region, China. Before particle size classification, the original kaolin sample consisted of 82.6% kaolinite, 12.3% quartz, 1.1% anatase, 0.6% rutile, 1.4% illite, and 2% other minerals (**Fig. 1)** as derived from Rietveld refinement of X-Ray Diffractograms.

The chemical composition of the raw kaolin sample was measured by X-ray Fluorescence (XRF), and the result is summarized in **Table 1**. It can be noted that the percentages of the main elements (Al_2O_3 and SiO_2) slightly deviate from the theoretical one predicted by the structural formula, confirming the relatively low purity of the kaolin sample inferred from XRD experiments.

2.2 Particle size classification of kaolinite

A series of settlement tests were carried out to obtain particle sizes under 2 μm. Kaolin (solid content: 20%) was dispersed in water with 1%wt sodium polyacrylate to obtain a slurry (Yang et al., 2020). The settling velocity *v* of the kaolinite in the kaolin slurry can be calculated according to Stokes' law:

$$v = \frac{gD^2(\rho_1 - \rho_2)}{18\mu} \quad (1)$$

$$v = \frac{H}{t} \quad (2)$$

$$D = \sqrt{\frac{18\mu H}{gt(\rho_1 - \rho_2)}} \quad (3)$$

where v is the settling velocity (mh^{-1}), g is the acceleration due to gravity ($9.80 ms^{-2}$), D is the equivalent sphere diameter of kaolinite (m), ρ_1 is the density of kaolinite (kgm^{-3}), ρ_2 is the density of the liquid, and μ is the viscosity of the slurry system ($kgm^{-1}s^{-1}$). H is the settling distance (m), and t is the settling time (h). Based on equation (1), the particle size of kaolinite is related to the settling time in the same viscosity system. Six barrels of kaolin slurry were prepared, and the settling time were fixed at 10 cm/1 h, 10 cm/2 h, 10 cm/3 h, 10 cm/5 h, 10 cm/10 h, and 10 cm/15 h (**Fig. S2 Supplementary material**).

All supernatants were collected by the siphon method, and part of it was kept for further analysis.

For size sorting kaolinite, vacuum filtration was performed as follows: first, a 200 nm membrane was used to filter the < 2 μm kaolin slurry. The filtered solution was referred to as A1. The solids on the membrane were recovered, mixed with an additional aqueous solution, and dispersed again by stirring for 30 min. This process was repeated three times to completely separate the particles from the suspension. A

450 nm membrane was then used to repeat the same filtering process. The filtered solution was referred to as A2, while the solids remaining on the membrane were referred to as A3. These three particle size fractions, A1, A2, and A3, were finally oven-dried at 105 ℃ for 24 h.

2.3 Sample characterization

The particle size distribution of kaolinite was evaluated using a laser particle size analyzer (Mastersizer 2000, Malvern, UK). Prior to analysis, the sample was sonicated for 5 minutes. Additional ultrasound was applied for 1 min in the injection cycle, whereas the total test time was 1~2min.

Small- and Wide-angle X-ray Scattering (SAXS and WAXS) experiments were performed to determine the microscale structure of kaolinite platelets. Aqueous suspension samples were sealed in cylindrical glass capillaries of 1.0 ± 0.1 mm diameter (Glas-Technik & Konstruktion, Germany). SAXS patterns were recorded at the SWING beamline of the SOLEIL synchrotron (Orsay, France) using fixed energy of 16keV (λ=0.777 Å) with two samples-to-detector distances of 0.5 m and 6 m. Bidimensional patterns were recorded on an Eiger detector. The radial integration of the scattering patterns yielded the

193 evolution of the scattered intensity versus scattering vector q, where q
194 is :
195 $$q = \frac{4\pi \sin\theta}{\lambda} \quad (4)$$
196 where: λ is the X-ray wavelength and θ is half the scattering angle. In
197 such conditions, the explored q range extends from 0.0008 $Å^{-1}$ to 2$Å^{-1}$.
198 XRD patterns of unoriented powders were measured using an X-ray
199 diffractometer (D8 Advance Bruker-AXS, Germany) with Cu$K\alpha$
200 radiation (λ=1.5405 Å). The diffraction patterns were tested over the
201 range of 2.5-70° (2θ) with a scan rate of 1°/min.
202 Brunauer–Emmet–Teller (BET) specific surface areas were deduced
203 from the nitrogen adsorption isotherm at 77 K using the BET surface
204 analyzer (Micromeritics ASAP 2460, U.S.A.). Before measurement,
205 each sample was evacuated under vacuum at 473 K for 2 h. The BET
206 surface area, total pore volume, average pore diameter, particle size,
207 pore width distribution, and micropore area are obtained from the
208 adsorption isotherms. The pore size distribution was acquired from the
209 desorption branch of the isotherm, supported by Kelvin's equation
210 (Kuila and Prasad, 2013).
211 The morphology of the samples was examined by scanning electron

212 microscopy (SEM, Hitachi SU8020, Japan) and high-resolution
213 transmission electron microscopy (HRTEM, JEOL-2010, 200 kV
214 Japan). Before TEM examination, the powder samples were dispersed
215 in ethanol solvent, and a drop of the suspension was deposited onto a
216 carbon film-coated copper grid to let the kaolinite particles precipitate
217 homogeneously. Selected-area electron diffraction (SAED) was
218 recorded with a point resolution of 0.18 nm.
219 ^{1}H, ^{29}Si, and ^{27}Al Magic angle spinning (MAS) nuclear magnetic
220 resonance (NMR) spectra were acquired on a Bruker Advance 500
221 spectrometer operating at Ω_L =500.50 MHz (^{1}H) and 99.43 MHz (^{29}Si)
222 with a 2.5 mm and 4 mm H-X MAS probe. Chemical shifts were
223 calibrated by the signal position of adamantane (1.85 ppm) for ^{1}H and
224 tetramethylsilane (TMS, 0 ppm) for ^{29}Si as external standards. The ^{1}H
225 experiment was examined under 90° pulse with a spinning rate of 14
226 kHz, with several scans of 512 and 1s of recycling delay. The ^{29}Si
227 experiment was performed under 90° pulse with a ^{1}H decoupling
228 spinal and was recorded at the same spinning rate. The number of
229 scans was 10240, and the recycling time was 10s. The decomposition
230 of the spectra was performed using Dmfit-2020 software. The spectra

were deconvoluted using mixed Gaussian/Lorentzian line fitting (Massiot et al., 2002; Quillard et al., 2011).

3. Results and discussion

3.1 Particle size classification of kaolinite by membrane separation

Filter membrane and vacuum filtration classify the kaolin slurry of < 2 μm into three particle size grades. **Fig. 2 (A)** reveals that such a classification is effective as three distinct peaks of particle size distribution can be observed in A1, A2, and A3 curves. A1 displays the smallest particle size, with an equivalent average sphere diameter of around 300 nm. This value is higher than that of the pores of the filter membrane used in the separation (200 nm), which can be assigned to the anisotropic nature of kaolin and/or to the partial aggregation of primary particles. The same trend is observed in the A2 sample, where the equivalent diameter of the largest particles (1000 nm) is higher than the membrane pore size (450 nm). **Fig. 2 (B)** displays the cumulative percentage frequency distributions for the three fractions. A2 particles are distributed in the 200~1000 nm range, whereas the size distribution for A3 particles ranges between 500 and

2000 nm.

3.2 Morphology

The reduction in particle size associated with size classification is clearly illustrated in the scanning electron micrographs (**Fig. 3**). A2 and A3 particles display a roughly hexagonal shape and significant size heterogeneity, whereas the smallest size fraction displays more homogeneous and rounded particles (**Fig. 3 (a)**). The sub-rounded platy shape suggests the existence of numerous crystalline defects that are particularly common in transported kaolinites. Compared with A2 (**Fig. 3 (b)**) and A3 (**Fig. 3 (c)**), the lateral distance between platelets in A1 is lower, and more gaps under 50 nm are visible. The kaolinite lamellae (**Fig. 3 (a)**) of A1 display a thickness of 50-300 nm and the stack of layers are linked to each other forming compact face-face associations after settling. This is in good agreement with Zbik and Gupta's observation (Gupta et al., 2011; Zbik et al., 2008).

Fig. S3 (Supplementary material) displays more selected TEM images of particles belonging to the three classes of kaolinite particles. In agreement with the SEM observations, the platelet size decreases from A3 to A1. The images also clearly reveal a turbostratic

arrangement of stacked crystallites. The selected area electron diffraction (SAED) pattern shown in **Fig. S3 (a)** confirms the disorder structure of kaolinite, and the rings correspond to the (020), (-130), (-113), (014), (3-11), and (-333) lattice plane.

3.3 XRD

XRD patterns of the raw kaolin sample are in good agreement with the standard PDF card of JCPDS 78-2110 (**Fig. 1**) and reveal the presence of some impurities that should be at least partially eliminated by sedimentation. Still, as revealed by the XRD patterns of the different classes (**Fig. 4**), significant amounts of mineral impurities are still present in the coarser fraction A3. Fraction A2 still contains small amounts of quartz, which likely corresponds to very fine particles. In contrast, the smallest fraction with an average particle size of 300 nm is completely devoid of any impurities, and the corresponding XRD pattern only exhibits kaolinite diffraction peaks (**Fig. 4**). Between 19° and 22° (2θ), the reflections (02*l*), (11*l*) are weak and broaden with decreasing particle size. These reflections are very sensitive to the abundance of translation defects, both random and specific displacements of type $\boldsymbol{t_1}$ (~-$\boldsymbol{a}$/3) and $\boldsymbol{t_2}$ (~-$\boldsymbol{a}$/3+$\boldsymbol{b}$/3) (Kogure et al.,

288 2010), and their weakening and broadening decrease the HI. The A1
289 sample, therefore, has low crystallinity and is the most disordered
290 among the three fractions. This may be due to either recrystallization
291 in low concentration solution or to weathering of large kaolinite
292 particles. Whereas all patterns display a decrease in the intensities of
293 all XRD reflections, the (060) peak at 61.5°-63° (2θ) is less affected
294 when kaolinite becomes more disordered. As shown by Brindley and
295 Kurtossy (1961), the $I_{(00l)}/I_{(060)}$ ratio (l=1 or 2) allows the evaluation of
296 the primary orientation of the disorder. In the case of sample A1, the
297 narrowing of the (060) reflection and broadening of the (001) indicate
298 a increasing dimensions along the ***b*** axis and decreasing along the ***c***
299 axis. This means that the finest particles have a higher aspect ratio.

300 **3.4 SAXS and WAXS**

301 **Fig. 5** displays the SAXS and WAXS results obtained by presenting
302 the evolution of the scattered intensity as a function of the scattering
303 vector q for the three size-sorted kaolinite samples. On a logarithmic
304 scale, the SAXS intensity dependence follows a power-law decay. At
305 high q, the three systems display a power law behavior where I scale
306 as $q^{-3.8}$ for the two larger sizes and as $q^{-3.7}$ for the smaller size. Such

behavior is close to Porod's law which states that the evolution for sharp interfaces should scale as q^{-4}. The deviation from Porod's law can be assigned to the surface roughness of the samples. In that context, the smallest particles appear to be slightly rougher than the two other classes. For A1 and A2 particles, a crossover towards a lower slope around q^{-2} is observed around 0.03 $Å^{-1}$ for A2 and 0.07 $Å^{-1}$ for A1. This indicates a scattering by slightly aggregated randomly oriented platelets with a high aspect ratio (Duijneveldt et al., 2005; Hotton et al., 2021; Pasco et al., 2021), which agrees with the TEM observations. For the smallest size (A1), the beginning of a Guinier plateau is observed for $q \approx 1.5\ 10^{-3}$ $Å^{-1}$. This suggests that the largest objects in this class of kaolinites have a size of around 4000 Å ($2\pi/1.5\ 10^{-3} Å^{-1}$) , which concurs with the laser diffraction results (**Fig. 2**).

In the high q-range from 0.5 to 2 $Å^{-1}$, the WAXS profiles provide information about the crystalline structure. A clear peak at $q \approx 0.88$ $Å^{-1}$ corresponds to a characteristic distance of 7.14 nm is observed. It can be assigned to the d(001) of kaolinite.

3.5 Adsorption isotherms

Fig. 6 shows the adsorption-desorption isotherms of N_2 at liquid N_2

(77 K) temperature for the three particle sizes. The shapes of the isotherm provide a qualitative assessment of the porous structure of the samples. Sample A3 displays an almost reversible Type II nitrogen isotherm. The isotherm shape indicates that this sample does mainly contain macropores, with non-existing micropores and few mesopores. Indeed, the hysteresis is extremely narrow, indicating the presence of a few large mesopores. The situation changes with decreasing particle size. Indeed, both A1 and A2 powders display significant hysteresis patterns without any plateau at high P/Po and can then be assigned to Type IV or Type IIB isotherms (Rouquerol et al., 2013). In such cases, the sample contains both mesopores accountable for the hysteresis and macropores, which explain the absence of any plateau at high relative pressure. The volume uptaken at P/Po near 1.0 indicates the total porosity of A1 and A2 for pore sizes < ~200 nm. As shown in **Table 2**, sample A1 has the most pores. Besides, it has more micropores than A2 powder, as shown by a larger adsorbed volume at an extremely low relative pressure (P/Po < 0.01).

The H3 hysteresis loop (according to IUPAC classification) of A1 and A2 are examples of Type II(b) isotherm, indicating the presence of

345 aggregates of plate-like particles.

346 **3.6 Specific surface area and pore size distribution**

347 The measured specific surface area values for A1 and A2 (40.65 and
348 27.13 m^2/g, respectively) exceed the range of 10~20 m^2/g of refined
349 natural kaolinite reported in the literature (Cases et al., 1986; Gregg
350 and Packer, 1954). The increase in the specific area of A1 and A2 is
351 mainly due to the decreased particle size of these fractions. For all
352 samples, the average particle size calculated from N_2-adsorption
353 (**Table 2)** is close to the size distribution deduced from laser
354 diffraction (**Fig. 2A and B**).

355 **Fig. 7** displays the BJH-HJ P_bSD (partial volume V of each pore
356 diameter D) obtained from the adsorption isotherm of the three
357 powders. The parameter dV/d (logD) is used to access the partial
358 porosity for each pore diameter range (Kuila and Prasad, 2013;
359 Mintova et al., 2015). For kaolinite powder A1, the distribution is
360 bimodal, with a major peak between 50~100 nm and a minor but
361 noticeable peak around 2~3 nm. Compared with A1, A2 displays a
362 similar pore size distribution, with the main peak located around
363 70~100 nm and the peak at 2~3 nm with lower intensity than in the

364 case of A1.

365 Combing the results of B.J.H. pore size distribution (**Fig. 7**) and pore
366 structure parameters (**Table 2**), it is clear that sample A1 had higher
367 BET, larger pore volume, and smaller average pore radius than
368 samples A2 and A3.

369 This variety of pore structures can be attributed to the presence of
370 more internal defects in ultrafine nano-kaolinite (**Fig. S3**).

371 **3.7 Solid-state NMR**

372 Solid-state NMR was used for probing the local environment and
373 short-range order in size-sorted kaolinites. ^{1}H MAS NMR spectra of
374 the three particle sizes of kaolinite were obtained at 500.5 MHz (**Fig.**
375 **8**). They can be decomposed into 6 or 7 Gaussian/Lorentzian peaks.
376 Peak 1 located at ~6.40 ppm, indicates the presence of residual water
377 in the three kaolinite samples (Zhu et al., 2016). A second peak at
378 4.3~4.5 ppm can be assigned to physically adsorbed water on the
379 external kaolinite surface. Both kinds of water will be easily
380 dehydrated overnight under a vacuum at 100 °C. In the range of
381 around 2 ppm, two peaks are observed at 2.79~2.65 ppm and at
382 1.81~1.80 ppm for the three samples of A1, A2 and A3. Peak 3 at

2.79~2.65 ppm is assigned to inner surface hydroxyls that form a hydrogen bond with oxygens from the SiO_4 tetrahedra, whereas peak 4 at 1.80 ppm corresponds to inner hydroxyls, with no linkage with any chemical groups in agreement with previously reported data (Fafard et al., 2017; Zhu et al., 2016). The integral areas (S) of peak 3 of A1, A2, and A3 are 38.48%, 21.31%, and 17.02%, respectively. S_{3A1}> S_{3A2}> S_{3A3} indicate that the degree of broken Al-O-Al and Si-O-Si bonds of particles evolve as A1> A2> A3. This seems to concur with the appearance of samples as observed by SEM and TEM. It must be pointed out that for an ideal $Al_2Si_2O_5(OH)_4$ kaolinite structure (Fafard et al., 2017), the ratio between the integrated signals of inner surface hydroxyl protons and inner hydroxyl protons should be 3:1 (**Fig. 8 (h)**). The ratios obtained for A1, A2, and A3 are significantly lower (0.97:1, 0.75:1, and 0.63:1, respectively), which may be attributed to the highly disordered structure and fine particle size of the studied kaolinite. In addition, these ratios decrease with increasing particle size, which suggests that the smaller the particles, the higher the number of hydroxyl groups.

In the range 0~2 ppm, the ^1H resonance peak displays two chemical

shifts (i) peak 5 around 1.3 ppm (1.38, 1.35 and 1.32 ppm for A1 to A3, respectively) assigned to $(Al_{VI})_2$-OH; (ii) peak 6 between 0 and 1 ppm (δ 0.85, 0.56 and 0.60 ppm for A1 to A3, respectively) assigned to the singly coordinated hydroxyl of Al_{VI}-OH (Huittinen et al., 2013). The integral areas of this latter signal for A1, A2, and A3 are 15.5%, 8.68%, and 9.97%, respectively, which proves again that A1 has the most edge hydroxyl groups. For the two large of A2 and A3, an additional strong, sharp signal exists at 1.01 ppm, which can be attributed to small isolated SiO_2 particles bearing hydrogen-bonded hydroxyl groups (Si-OH-Si) (Viani et al., 2017).

The ^{29}Si NMR spectra between -90~ -92.5 ppm can be decomposed into three components. A weak one located at about -89 ppm can be assigned to Q^3(1Al) (Cadars et al., 2012; Magi et al., 1984; Thompson, 1984) and corresponds to the presence of one tetrahedral Al connected to three tetrahedral silicon atoms via bridging oxygen atoms, and to the octahedral sheet by an apical oxygen atom (see details in **Fig. 10**). The relative intensity of this signal increases with diminishing particle size. Considering that the radius of Al^{3+}(IV) (0.39 Å) is larger than that of Si^{4+} (Radii=0.26 Å), the presence of more Al for Si substitution

421 in the finest particles could explain at least partially the high degree of
422 disorder displayed by A1 particles. At a slightly lower chemical shift,
423 all samples exhibit a wide signal that can be decomposed into two
424 components with almost equal intensities (see **Fig. 8 (b), (d), and (f)**)
425 that are both ascribed to Q^3(0Al). The fact that the signal is split in two
426 reveals that Si sites in SiO_4 tetrahedrons, i.e., are not strictly equivalent,
427 which agrees with previous studies (Magi et al., 1984; Thompson et al.,
428 1992). In addition, samples A2 and A3 display additional resonances
429 at δ -107.23 ppm and -107.17 ppm that correspond to Q_4 signals
430 assigned to the presence of silica impurities.
431 The ^{27}Al NMR spectra (**Fig. 9**) display a strong peak at δ=3 ppm
432 assigned to six-coordinated Al (Al(VI)) and a much weaker signal at
433 δ=70 ppm assigned to Al(IV) (Newman et al., 1994; Thompson, 1984).
434 This latter signal is rather weak in agreement with the structure of
435 kaolinite, but its intensity increases with decreasing particle size,
436 which confirms the results obtained from the analysis of ^{29}Si spectra,
437 i.e., that Al for Si substitution is more important in smaller particles.

438 **4. Conclusion**

439 Three different particle sizes of kaolinite were separated from high-

defect raw sedimentary kaolin through sedimentation and vacuum membrane filtration, that is, A1 (<300 nm), A2 (200~1000 nm), and A3 (500~2000 nm). The comprehensive studies reveal that the degree of the structural disorder of kaolinite increases as the particle size decreases. The smallest particle size of kaolinite possessed high degrees of broken Al-O-Al and Si-O-Si bonds, a more disordered structure, and an elevated specific surface area. The high disorder degree of tiny kaolinite crystals can be attributed to the more aluminum substituted for silicon in the tetrahedron sheet of their structure, compared to the coarser kaolinite crystals.

Acknowledgment

This work thanks the financial support of the National Key R&D Program of China (No. 2019YFC1904903) and the Science and Technology Major Projects of Shanxi Province of China (No. 20181101003). Yongjie Yang thanks the support provided by the China Scholarship Council (CSC No. 202006430032) during his visit to Sorbonne Université.

References

Aparicio, P., 1999. Mineralogical Interference on Kaolinite Crystallinity Index Measurements. Clays and Clay Minerals 47, 12-27.

Awad, M.E., López-Galindo, A., Sánchez-Espejo, R., Sainz-Díaz, C.I., El-Rahmany, M.M., Viseras, C., 2018. Crystallite size as a function of kaolinite structural order-disorder and kaolin chemical variability: Sedimentological implication. Applied Clay Science 162, 261-267.

Bish, D.L., 1993. Rietveld Refinement of the Kaolinite Structure at 1.5 K. Clays and Clay Minerals 41, 738-744.

Brindley, G., Kao, C.-C., Harrison, J., Lipsicas, M., Raythatha, R., 1986. Relation between structural disorder and other characteristics of kaolinites and dickites. Clays and Clay Minerals 34, 239-249.

Brindley, G., Kurtossy, S.S., 1961. Quantitative determination of kaolinite by X-ray diffraction. American Mineralogist: Journal of Earth Planetary Materials 46, 1205-1215.

Cadars, S., Guégan, R., Garaga, M.N., Bourrat, X., Le Forestier, L., Fayon, F., Huynh, T.V., Allier, T., Nour, Z., Massiot, D., 2012. New Insights into the Molecular Structures, Compositions, and Cation Distributions in Synthetic and Natural Montmorillonite Clays. Chemistry of Materials 24, 4376-4389.

Cases, J., Cunin, P., Grillett, Y., Poinsignon, C., Yvon, J., 1986. Methods of analysing morphology of kaolinites: relations between crystallographic and morphological properties. Clay minerals 21, 55-68.

Cheng, P., Schachman, H., 1955. Studies on the validity of the Einstein viscosity law and Stokes' law of sedimentation. Journal of polymer science 16, 19-30.

Du, J., Morris, G., Pushkarova, R.A., Smart, R.S., 2010. Effect of surface structure of kaolinite on aggregation, settling rate, and bed density. Langmuir 26, 13227-13235.

Duijneveldt, J.S.v., Klein, S., Leach, E., Pizzey, C., Richardson, R.M., 2005. Large scale structures in liquid crystal/clay colloids. Journal of Physics: Condensed Matter 17, 2255-2267.

Eshel, G., Levy, G., Mingelgrin, U., Singer, M., 2004. Critical evaluation of the use of laser diffraction for particle-size distribution analysis. Soil Science Society of America Journal 68, 736-743.

Fafard, J., Terskikh, V., Detellier, C., 2017. Solid-state 1H and 27Al NMR studies of DMSO-kaolinite intercalates. Clays and Clay Minerals 65, 206-219.

Franco, F., Perez-Maqueda, L.A., Perez-Rodriguez, J.L., 2004a. The effect of ultrasound on the particle size and structural disorder of a well-ordered kaolinite.

Journal of colloid and interface science 274, 107-117.
Franco, F., Pérez-Maqueda, L.A., Pérez-Rodríguez, J.L., 2004b. Influence of the particle-size reduction by ultrasound treatment on the dehydroxylation process of kaolinites. J Therm Anal Calorim 78, 1043-1055.
Gregg, S., Packer, R., 1954. The production of active solids by thermal decomposition. Part IV. Vermiculite. Journal of the Chemical Society, 3887-3893.
Gupta, V., Hampton, M.A., Stokes, J.R., Nguyen, A.V., Miller, J.D., 2011. Particle interactions in kaolinite suspensions and corresponding aggregate structures. Journal of colloid and interface science 359, 95-103.
Hamzaoui, R., Muslim, F., Guessasma, S., Bennabi, A., Guillin, J., 2015. Structural and thermal behavior of proclay kaolinite using high energy ball milling process. Powder Technology 271, 228-237.
Hotton, C., Sirieix-Plenet, J., Ducouret, G., Bizien, T., Chenneviere, A., Porcar, L., Michot, L., Malikova, N., 2021. Organisation of clay nanoplatelets in a polyelectrolyte-based hydrogel. Journal of colloid and interface science 604, 358-367.
Huittinen, N., Sarv, P., Lehto, J., 2013. A 1H and 27Al NMR investigation of yttrium(III) and europium(III) interaction with kaolinite. Applied Clay Science 80-81, 182-188.
Jaber, M., Lambert, J.-F., Balme, S., 2018. Protein adsorption on clay minerals, Surface and Interface Chemistry of Clay Minerals, pp. 255-288.
Kobayashi, Y., Sumi, K., Kato, E., 2000. Preparation of dense cordierite ceramics from magnesium compounds and kaolinite without additives. Ceramics International 26, 739-743.
Kogure, T., Elzea-Kogel, J., Johnston, C.T., Bish, D.L., 2010. Stacking Disorder in a Sedimentary Kaolinite. Clays and Clay Minerals 58, 62-71.
Konert, M., Vandenberghe, J., 1997. Comparison of laser grain size analysis with pipette and sieve analysis: a solution for the underestimation of the clay fraction. Sedimentology 44, 523-535.
Kuila, U., Prasad, M., 2013. Specific surface area and pore-size distribution in clays and shales. Geophysical Prospecting 61, 341-362.
Liu, L., Liu, Q., Algeo, T., Zhang, H., Yang, Y., Peng, G., Zhang, S., Hong, H., Liu, D., 2021. Mineralogy, Geochemistry, and Genesis of Kaolinitic Claystone Deposits in the Datong Coalfield, Northern China. Clays and Clay Minerals 69, 68-93.
Magi, M., Lippmaa, E., Samoson, A., Engelhardt, G., Grimmer, A., 1984. Solid-state high-resolution silicon-29 chemical shifts in silicates. The Journal of Physical Chemistry 88, 1518-1522.
Makó, É., Frost, R.L., Kristóf, J., Horváth, E., 2001. The Effect of Quartz Content on

the Mechanochemical Activation of Kaolinite. Journal of colloid and interface science 244, 359-364.
Massiot, D., Fayon, F., Capron, M., King, I., Le Calvé, S., Alonso, B., Durand, J.-O., Bujoli, B., Gan, Z., Hoatson, G., 2002. Modelling one- and two-dimensional solid-state NMR spectra. Magnetic Resonance in Chemistry 40, 70-76.
Mintova, S., Jaber, M., Valtchev, V., 2015. Nanosized microporous crystals: emerging applications. Chemical Society Reviews 44, 7207-7233.
Morsy, F.A., El-Sherbiny, S., Hassan, M.S., Mohammed, H.F., 2014. Modification and evaluation of Egyptian kaolinite as pigment for paper coating. Powder Technology 264, 430-438.
Mpofu, P., Addai-Mensah, J., Ralston, J., 2003. Investigation of the effect of polymer structure type on flocculation, rheology and dewatering behaviour of kaolinite dispersions. International Journal of Mineral Processing 71, 247-268.
Newman, R., Childs, C., Churchman, G., 1994. Aluminium coordination and structural disorder in halloysite and kaolinite by 27Al NMR spectroscopy. Clay Minerals 29, 305-312.
Pasco, H., de Viguerie, L., Faustini, M., Coelho-Diogo, C., Ersen, O., Gervais, C., Gobeaux, F., Ihiawakrim, D., Jaber, M., Walter, P., Sanchez, C., 2021. Shedding Light on Functional Hybrid Nanocomposites 19th Century Paint Medium. Advanced Functional Materials.
Plançon, A., Giese, R., Snyder, R., Drits, V., Bookin, A., 1989. Stacking faults in the kaolin-group minerals: Defect structures of kaolinite. Clays and Clay Minerals 37, 203-210.
Quillard, S., Paris, M., Deniard, P., Gildenhaar, R., Berger, G., Obadia, L., Bouler, J.M., 2011. Structural and spectroscopic characterization of a series of potassium- and/or sodium-substituted beta-tricalcium phosphate. Acta Biomater 7, 1844-1852.
Rand, B., Melton, I.E., 1977. Particle interactions in aqueous kaolinite suspensions: I. Effect of pH and electrolyte upon the mode of particle interaction in homoionic sodium kaolinite suspensions. Journal of colloid and interface science 60, 308-320.
Richard, D., Rendtorff, N.M., 2019. First principles study of structural properties and electric field gradients in kaolinite. Applied Clay Science 169, 67-73.
Rouquerol, J., Rouquerol, F., Llewellyn, P., Maurin, G., Sing, K.S., 2013. Adsorption by powders and porous solids: principles, methodology and applications. Academic press.
Silva, F.A.N.G., Luz, A.B., Sampaio, J.A., Bertolino, L.C., Scorzelli, R.B., Duttine, M., da Silva, F.T., 2009. Technological characterization of kaolin: Study of the case of the Borborema–Seridó region (Brazil). Applied Clay Science 44, 189-193.
Suraj, G., Iyer, C., Rugmini, S., Lalithambika, M., 1997. The effect of micronization

573 on kaolinites and their sorption behaviour. Applied Clay Science 12, 111-130.
574 Thompson, J., 1984. 29 Si and 27 Al nuclear magnetic resonance spectroscopy of 2:
575 1 clay minerals. Clay minerals 19, 229-236.
576 Thompson, J.G., Uwins, P.J., Whittaker, A.K., Mackinnon, I.D., 1992. Structural
577 characterisation of kaolinite: NaCl intercalate and its derivatives. Clays and Clay
578 Minerals 40, 369-380.
579 Varajão, A.F.D.C., Gilkes, R.J., Hart, R.D., 2001. The relationships between kaolinite
580 crystal properties and the origin of materials for a Brazilian kaolin deposit. Clays and
581 Clay Minerals 49, 44-59.
582 Viani, A., Mali, G., Mácová, P., 2017. Investigation of amorphous and crystalline
583 phosphates in magnesium phosphate ceramics with solid-state 1 H and 31 P NMR
584 spectroscopy. Ceramics International 43, 6571-6579.
585 Wen, B., Aydin, A., Duzgoren-Aydin, N.S., 2002. A comparative study of particle
586 size analyses by sieve-hydrometer and laser diffraction methods. Geotechnical
587 Testing Journal 25, 434-442.
588 Yang, X., Zhang, Q., Li, X., Jia, X., Wei, X., Shao, M.a., 2015. Determination of Soil
589 Texture by Laser Diffraction Method. Soil Science Society of America Journal 79,
590 1556-1566.
591 Yang, Y., Zhang, H., Zhang, K., Liu, L., Ji, L., Liu, Q., 2020. Vulcanization,
592 interfacial interaction, and dynamic mechanical properties of in-situ organic amino
593 modified kaolinite/SBR nanocomposites based on latex compounding method.
594 Applied Clay Science 185.
595 Zbik, M.S., Smart, R.S., Morris, G.E., 2008. Kaolinite flocculation structure. Journal
596 of colloid and interface science 328, 73-80.
597 Zhang, K., Zhang, H., Liu, L., Yang, Y., Liu, L., Liu, Q., 2021a. Dispersibility of
598 Kaolinite-Rich Coal Gangue in Rubber Matrix and the Mechanical Properties and
599 Thermal Stability of the Composites. Minerals 11.
600 Zhang, S., Liu, Q., Yang, Y., Wang, D., He, J., Sun, L., 2017. Preparation,
601 morphology, and structure of kaolinites with various aspect ratios. Applied Clay
602 Science 147, 117-122.
603 Zhang, S., Liu, Q., Yang, Y., Zhang, H., Liu, J., Zeng, S., LaChance, A.M., Barrett,
604 A.T., Sun, L., 2021b. An efficient method to prepare aluminosilicate nanoscrolls
605 under mild conditions. Chem Commun (Camb) 57, 789-792.
606 Zhang, Y., Liu, Q., Zhang, Q., Lu, Y., 2010. Gas barrier properties of natural
607 rubber/kaolin composites prepared by melt blending. Applied Clay Science 50, 255-
608 259.
609 Zhu, X., Zhu, Z., Lei, X., Yan, C., 2016. Defects in structure as the sources of the
610 surface charges of kaolinite. Applied Clay Science 124-125, 127-136.

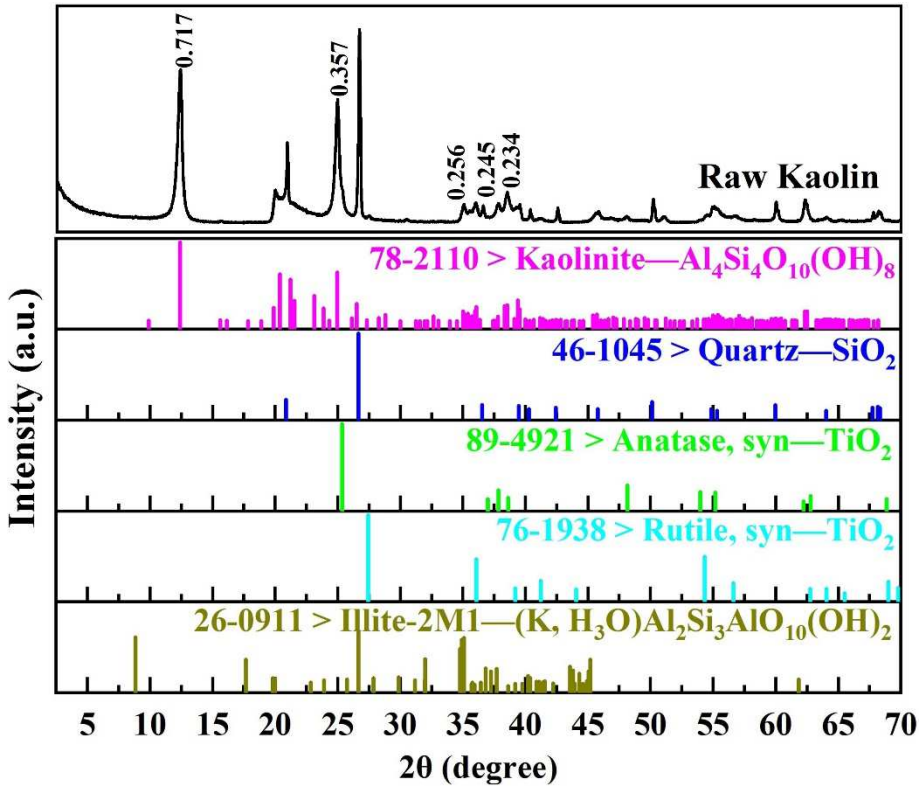

Fig. 1. XRD patterns of raw kaolin sample.

620

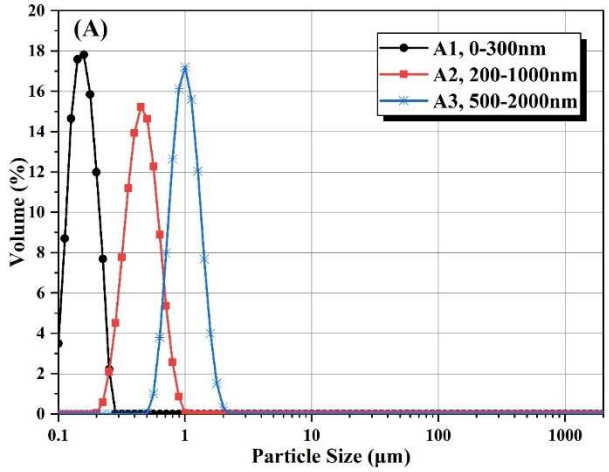

621

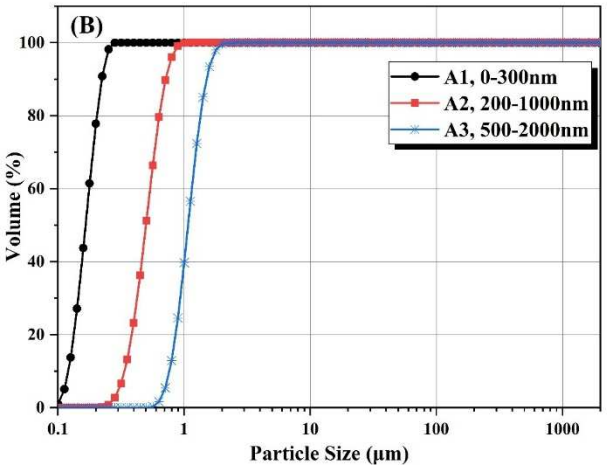

622 **Fig. 2.** Particle size distribution (A) and cumulative particle size distribution (B) of
623 kaolinite after vacuum filtration of the < 2 μm kaolin suspension.

624

625

626

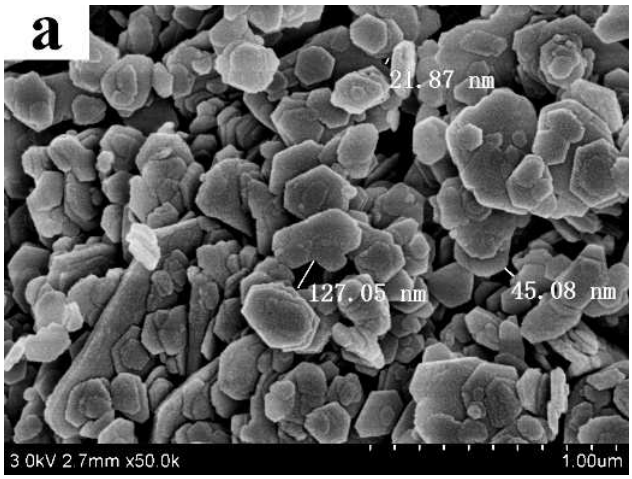

627

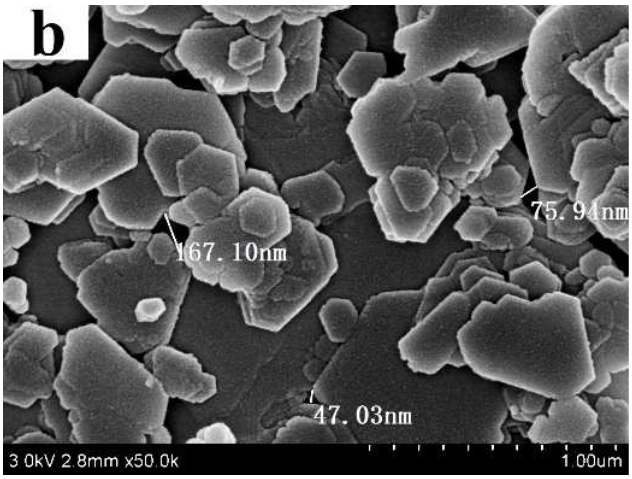

628

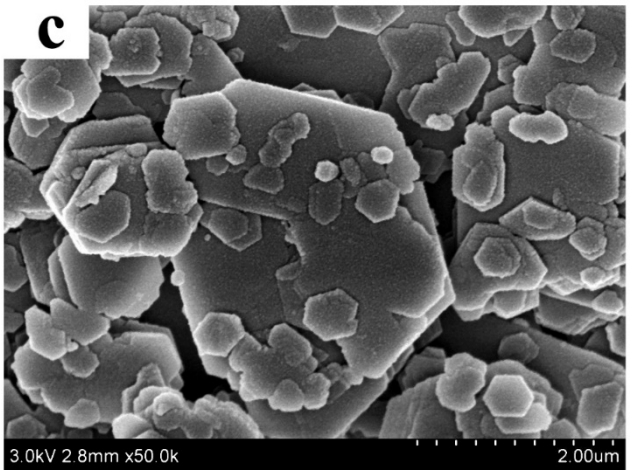

629 **Fig. 3.** SEM observations of three different particle sizes of kaolinite; (a) A1; (b) A2;
630 (c) A3.

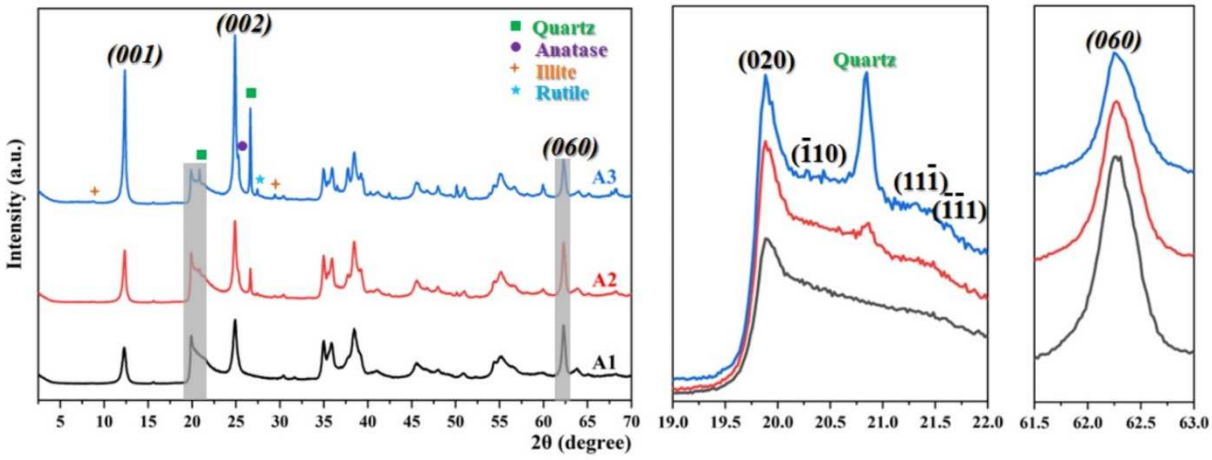

Fig. 4. XRD patterns of kaolinite samples classified into different particle sizes; A1 ≤300 nm, A2 200~1000 nm, A3 500~2000 nm.

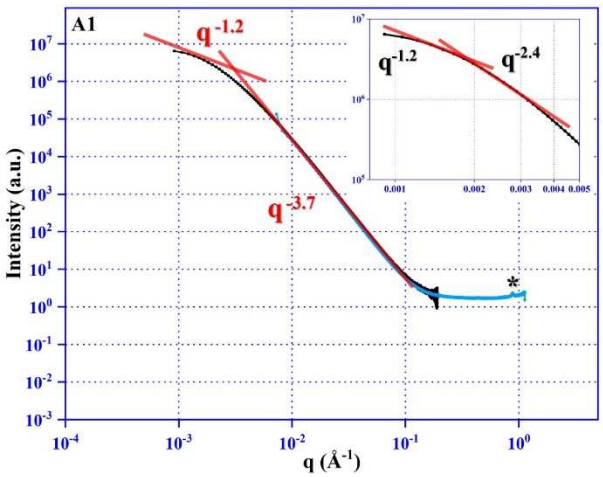

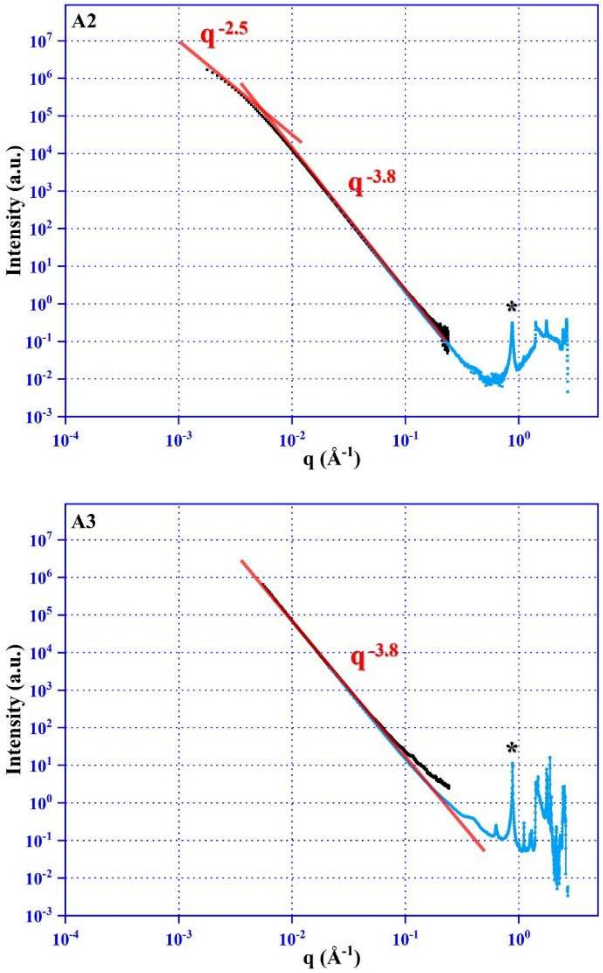

Fig. 5. Small- and Wide-angle scattering curves were obtained from SAXS and WAXS.

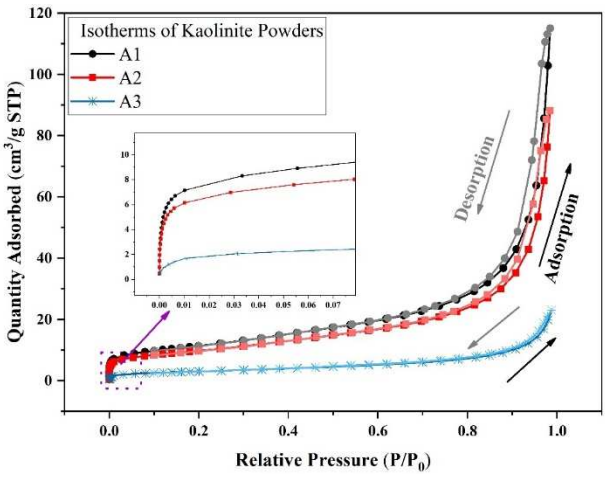

Fig. 6. Adsorption-desorption isotherms of N_2 at liquid N_2 (77 K) temperature of three particle size distributions of A1, A2, and A3.

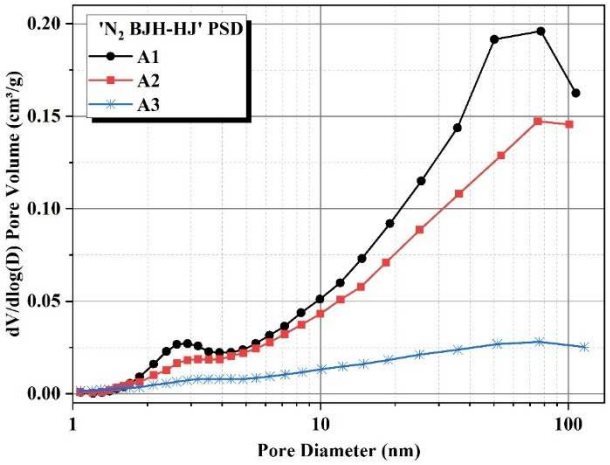

Fig. 7. BJH-HJ P_bSD of A1, A2, and A3 acquired from the N_2 adsorption isotherm; Sample A1 and A2 have bimodal distribution with a minor peak around 2~3 nm, while A1 has a major peak at 50-100 nm and A2 at 70~100 nm. A3 shows a unimodal distribution with a very weak peak around 100 nm.

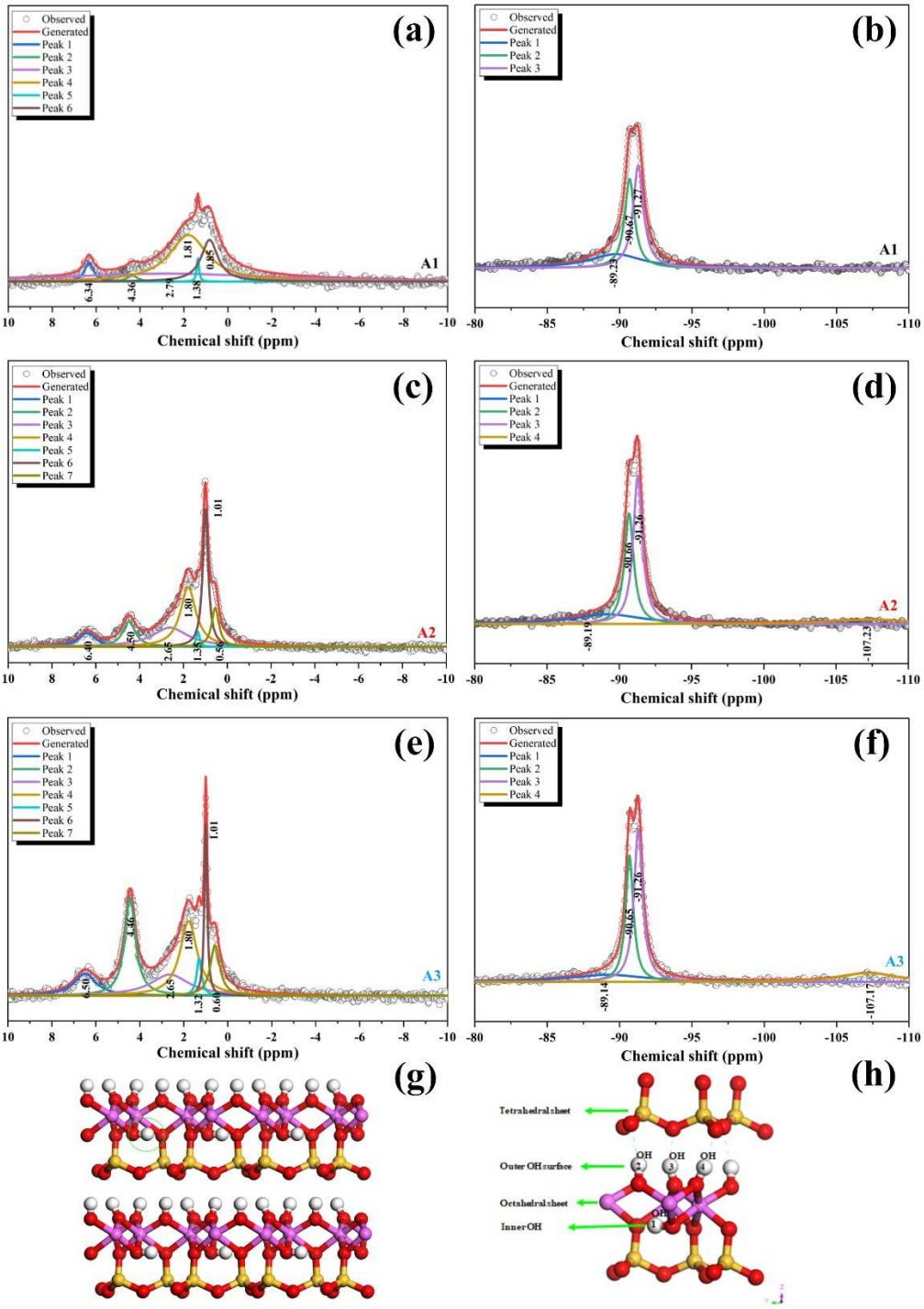

Fig. 8. ^{1}H (left) and ^{29}Si (right) MAS NMR spectra of A1, A2, and A3.

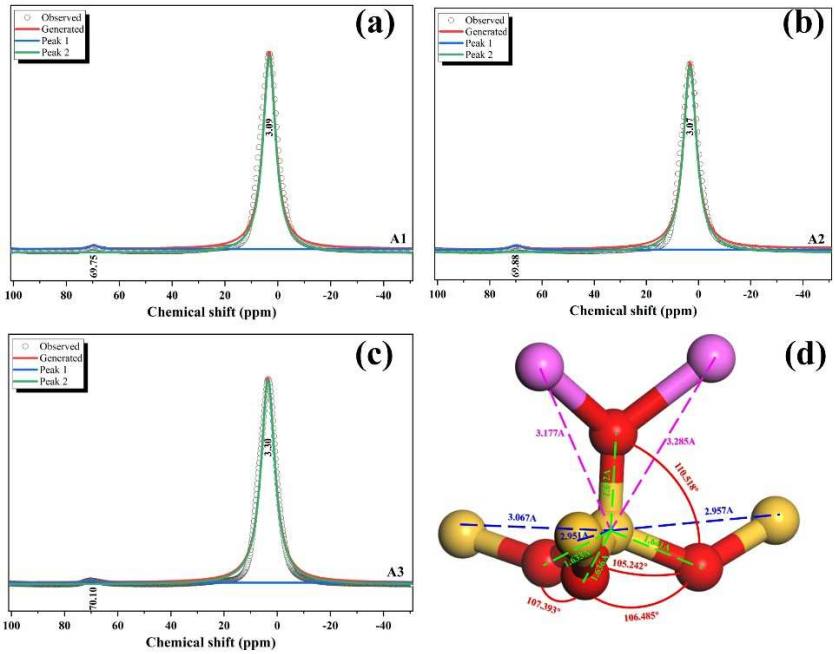

Fig. 9. ^{27}Al MAS NMR spectra of A1, A2, and A3.

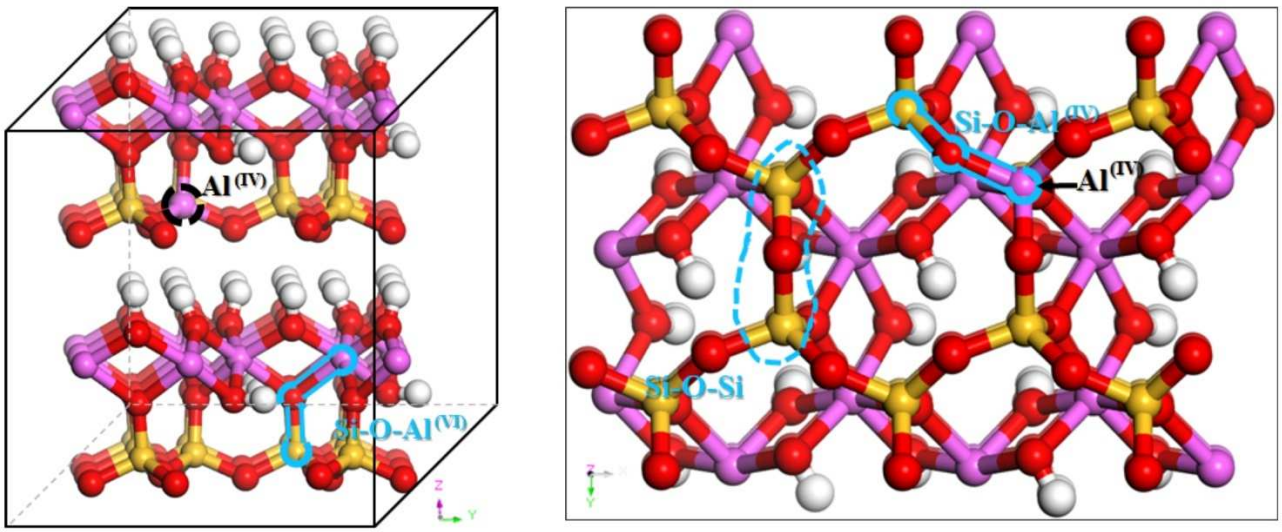

Fig. 10. Projection of the structure of kaolinite from the (100) direction, which contains one Q^3(1Al) Si moieties per unit cell.

672 **Table 1** Chemical composition of original kaolin in the study (wt%) .

Sample	SiO_2	Al_2O_3	TiO_2	Fe_2O_3	P_2O_5	K_2O	CaO	MgO	SO_3	Cr_2O_3	LOI
Kaolin	49.92	31.29	1.79	1.15	0.16	0.12	0.09	0.09	0.06	0.027	15.1

673
674
675
676
677 **Table 2** BET and pore structure parameters of three different particle
678 sizes of kaolinite.

	[c]BET Surface Area (m^2/g)	[a]Pore Volume (cm^3/g)	[b]Pore size (nm)	[c]Nanoparticle Size (Average Particle Size, nm)
A1	40.6572	0.178006	17.51289	147.5753
A2	27.1262	0.136377	15.67295	430.963
A3	11.0345	0.035655	10.92476	1087.4934

679
680 a: Single point adsorption total pore volume of pores less than 127.7428 nm
681 diameter at p/p° of A1= 0.984750664;
682 Single point adsorption total pore volume of pores less than 122.8734 nm
683 diameter at p/p° of A2= 0.984134123;
684 Single point adsorption total pore volume of pores less than 160.7880 nm
685 diameter at p/p° of A3 = 0.987934275;
686 b: Adsorption average pore diameter (4V/A by B.E.T.);
687 c: Average Particle Size.
688